



Research Article

## S-Scheme ZnO/g-C<sub>3</sub>N<sub>5</sub> Visible Light Active Photocatalyst for Rhodamine B Dye Degradation and Hg Sensing Applications

Roopashree Bangalore Nagesh, Gurushantha Kariyanna\* and Nagaraju Kottam  
Department of Chemistry, M. S. Ramaiah Institute of Technology (affiliated to VTU), Bengaluru, India

Ashly Panichithadathil Chandran  
Department of Chemistry, Sir M. Visvesvaraya Institute of Technology, Bengaluru, India

Meena Subramaniam  
Department of Chemistry, Dayananda Sagar College of Engineering, Bengaluru, India

Keshavamurthy Kempaiah  
Department of Physics, Dayananda Sagar College of Engineering, Bengaluru, India

Raghu Gunigollahalli Kempegowda  
Department of Chemistry, Siddaganga Institute of Technology, Tumakuru, India

Atthasit Tawai  
The Sirindhorn International Thai-German Graduate School of Engineering, Biorefinery and Process Automation Engineering Center (BPAEC), King Mongkut's University of Technology North Bangkok, Bangkok, Thailand

\* Corresponding author. E-mail: gurushanthak2016@gmail.com DOI: 10.14416/j.asep.2025.06.001  
Received: 9 January 2025; Revised: 4 March 2025; Accepted: 2 May 2025; Published online: 4 June 2025  
© 2025 King Mongkut's University of Technology North Bangkok. All Rights Reserved.

### Abstract

The main focus of the current work, the host material (ZnO and g-C<sub>3</sub>N<sub>5</sub> NPs) and its composites (ZnO/g-C<sub>3</sub>N<sub>5</sub>) were synthesized by precipitation and hydrothermal methods using zinc nitrate and melamine. The final materials were exposed to photocatalytic and electrochemical activities after being thoroughly characterized by PXRD, UV-visible DRS Spectroscopy, FT-IR, XPS, SEM-EDS, and TEM. There are diffraction peaks in the PXRD pattern that belong to both the ZnO and g-C<sub>3</sub>N<sub>5</sub> samples. The estimated band gap energy decreases from 3.08 (ZnO) to 2.74 ZnO/g-C<sub>3</sub>N<sub>5</sub> eV. The ZnO/g-C<sub>3</sub>N<sub>5</sub> shows enhanced photocatalytic activity of 97.53% for degradation of RhB dye in visible light irradiation. Further, the ZnO/g-C<sub>3</sub>N<sub>5</sub> composite material is a selective modifier pattern for mercury detection. This synthesized material shows better sensitivity at the lowest detection limit of 1nM. Hence, this work shows the novel synthesis for the effective photocatalyst for water treatment and as an efficient sensor for the detection of mercury levels in the wastewater.

**Keywords:** Electrochemical sensor, Nanocomposite, Photocatalytic degradation, S-scheme heterojunction

### 1 Introduction

Environmental degradation and the energy crisis are the two major issues that human society is currently facing [1]. Dyes and their byproducts' contaminants in

paper, leather, dyeing, and textile industries pose a concern to the environment today. The primary effects on the ecosystem may be caused by the disposal of either poorly metabolized or insufficiently absorbed live organisms. These important problems could be



resolved by a number of practical methods, including biological therapy, adsorption and photocatalysis [2].

Rhodamine B is a xanthene cationic dye of green crystals or reddish-violet powder widely used in the paper printing industry and as a food and textile coloring stuff. It is dangerous for individuals as well as animals since it irritates the skin, eyes, and respiratory system when ingested. Medical research has demonstrated that drinking water tainted with Rhodamine B dye is extremely neurotoxic, carcinogenic, and chronic. Therefore, before being released into water streams, wastewater that has been tainted with Rhodamine B dye needs to be thoroughly treated [3]. There is great potential for semiconductor photocatalytic technology to convert sustainable solar energy into chemically storable energy, with important implications for the energy and environmental domains. Nevertheless, the performance of individual photocatalysts is limited by the intrinsic problem of fast recombination of holes and electrons produced by photolysis [4]. Semiconductor photocatalysis and photovoltaics use two types of heterojunctions: S-scheme and Z-scheme. Each has its advantages and works well in certain situations. S-scheme heterojunctions offer several advantages over Z-scheme configurations, including enhanced charge separation, simplified structure, higher efficiency, broader material compatibility, and tunable energy levels. These attributes make them promising candidates for a range of uses in environmental restoration and energy conversion [5].

Building 2D S-scheme heterojunction photocatalysts appears to be a successful method for overcoming this obstacle. A significant interfacial area is guaranteed by the purposeful design of dimensionality, and the charge transfer mechanism of the S-scheme maximizes redox capabilities and enables effective charge separation [6]. The interface between two distinct semiconductor materials with different bandgaps is known as a heterojunction, and it is commonly seen in electrical and optoelectronic devices. It is common practice to select materials on either side of the junction based on their unique electrical features, such as different band structures, optical traits, or electron mobility [7]. The conduction and valence bands of the two materials aligned in a heterojunction can produce special qualities like the creation of particular light emission properties or the confinement of electrons or holes.

An “S-shaped” band structure at the interface between the two materials is a characteristic of the S-scheme heterojunction. This band alignment results

from the formation of a potential barrier at the interface caused by the materials' differing electron affinities, which affects charge transport across the junction. A Z-scheme heterojunction creates a “Z-shaped” pathway for charge carriers by aligning the energy levels (conduction and valence bands) of the two materials so that electrons and holes move through the heterojunction in two steps. Effective charge separation is usually made possible by one substance acting as the electron acceptor and the other as the hole acceptor [8].

The potential applications of large band gap semiconductor metal oxide nanoparticles to efficiently degrade different organic contaminants have been highlighted in numerous studies. Unfortunately, a disadvantage of many oxide materials employed in degrading processes is that they need high-energy light sources [9]. Researchers have developed alternative approaches to tackle this issue. Creating photocatalysts that oxidize organic pollutants over visible light has become more popular as a means of reducing the risk of ultraviolet (UV) light-induced cancer [10].

The catalyst should also exhibit high levels of chemical and physical stability and be non-toxic. The promising photocatalyst graphitic carbon nitride ( $g\text{-C}_3\text{N}_5$ ) is widely utilized in wastewater treatment because of its robust sensitivity to visible light, narrow bandgap, and stable chemical characteristics [11]. However, the tiny area of contact and fast photoelectron-hole recombination pace of  $g\text{-C}_3\text{N}_5$  has restricted its use in the field of photocatalytic degradation [12]. The  $g\text{-C}_3\text{N}_5$ 's photocatalytic performance is further enhanced by modification techniques such as the loading of noble metals, element doping, morphological regulation, and heterojunction construction. Among the several semiconductor materials, ZnO has drawn a lot of interest [13]. ZnO reacts strongly to UV light and has broad band gap energy. However, the quick photo electron-hole recombination rate of ZnO limits its large-scale use in photocatalytic degradation [14]. Hence ZnO and  $g\text{-C}_3\text{N}_5$  are combined to make ZnO/ $g\text{-C}_3\text{N}_5$ , which exhibits strong photocatalytic activity over visible light.

The development of an electrochemical interface composed of a selective modifiers motif that shows a potential affinity for a specific metal ion is highly desirable in the field of ion selective sensors [15]. Mercury ( $\text{Hg}^{2+}$ ) is regarded as one of the most dangerous and extensively spread environmental pollutants [16]. Exposure to this ion, even at trace

concentration levels, may have detrimental effects on aquatic and biological systems [17]. The World Health Organization (WHO) has established that two parts per billion is the maximum threshold limit value (TLV) that can be applied to drinkable water [18]. Many techniques have been documented and proven for determining metal ions more specifically mercury ions [19]. Among the methods, electrochemical methods have gained tremendous interest due to their ease of operation, low day-to-day maintenance costs, possibility of achieving low detection limits and mainly their field applicability which is adequately needed for practical industrial analytical applications [20]. In electrochemical methods, the selection of modifier motif acts as a deciding factor in achieving selectivity thereby sensitivity [21]. Owing to this, various sensor interfaces for mercury electrochemical determination have been documented in the literature [22]. Thin film-based electrodes have garnered significant attention because of their surface renewability and ease of manufacture [23]. Therefore, there is a pressing need for the introduction of a new interface with high sensitivity and selectivity to ensure the levels of mercury to be within the WHO's recommended limits [24].

There were numerous papers available for the ZnO/g-C<sub>3</sub>N<sub>4</sub> composite, but just a few for the heterojunction ZnO/g-C<sub>3</sub>N<sub>5</sub> composite having photocatalytic activity. Jia *et al.*, reported that, in comparison to pure ZnO, g-C<sub>3</sub>N<sub>5</sub>, Ce-CN, and ZN/CN, the ZN/Ce-CN heterojunction photocatalyst demonstrated superior photocatalytic activity for methylene blue, with a degradation rate of up to 97% at 90 min [25]. Energy storage, photocatalysis, and environmental protection are just a few of the many uses for the ZnO/g-C<sub>3</sub>N<sub>5</sub> nanomaterial. These benefits include increased photocatalytic activity (e.g., water splitting, CO<sub>2</sub> reduction, organic pollutant degradation due to absorption of visible light and increased charge separation), improved chemical stability, increased surface area and porosity due to nanostructured materials, improved electron transfer, synergy in pollutant degradation, improved solar energy conversion for photovoltaic and energy harvesting applications, sensing and energy storage applications, low cost, and eco-friendliness. Also, they are non-toxic in nature with tunable properties. Thus, in the current study, we developed a ZnO/g-C<sub>3</sub>N<sub>5</sub> (Figure 1) composite-based thin-film sensor that can measure Hg<sup>2+</sup> at low concentrations with precision and focus while minimizing interference and maintaining electrochemical activity. This sensor will then be used

to measure the mercury content of real samples and examine the degradation of Rhodamine B dye through photocatalysis.

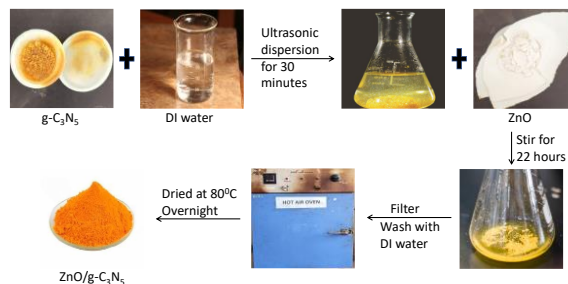


**Figure 1:** Scheme for the preparation of ZnO/g-C<sub>3</sub>N<sub>5</sub> nanocomposites.

## 2 Materials and Techniques

### 2.1 Materials

Zinc nitrate hexahydrate [Zn(NO<sub>3</sub>)<sub>2</sub>·6H<sub>2</sub>O], ammonium hydroxide [NH<sub>4</sub>OH], melamine [C<sub>3</sub>H<sub>6</sub>N<sub>6</sub>], hydrazine hydrate [H<sub>4</sub>N<sub>2</sub>·H<sub>2</sub>O], hydrochloric acid [HCl], sodium hydroxide [NaOH], ethanol [C<sub>2</sub>H<sub>5</sub>OH] and Rhodamine B [C<sub>28</sub>H<sub>31</sub>ClN<sub>2</sub>O<sub>3</sub>] were purchased from SD Fine Chemicals. All the reagents were of analytical grade and used as received without further purification. All solutions were prepared using deionized water from a Milli-Q water purifier (resistivity 18.2 MΩ cm<sup>-1</sup> at 25 °C) and adjusted to the desired pH. For sensor studies, the stock solutions of saturated concentrations of mercury (Hg) using mercuric bromide were prepared and kept for storage in the refrigerator. Working standards aliquots were prepared on the day of the experiment by diluting calculated amounts of aliquots from the stock solution.

### 2.2 Methods

#### 2.2.1 Synthesis of ZnO

Precipitation and calcinations were used to prepare zinc oxide nanomaterials. A 0.2 M solution of zinc nitrate hexahydrate was prepared, and then 50% ammonium hydroxide solution was added in drop slowly under continuous stirring to arrive at pH 10 [26]. Following centrifugation, the precipitate formed by the interaction of the zinc nitrate with the ammonium hydroxide solution was collected at 6000 rpm for 15 mins. The precipitate was washed four times using deionized water to get rid of the



contaminants. Next, the final products were dried for six hours in an oven at 80 °C.

### 2.2.2 Synthesis of *g*-C<sub>3</sub>N<sub>5</sub>

#### *Synthesis of Melem (2, 5, 8 – triamino – s – heptazine)*

Melem was made by heating 6 g of melamine at 425 °C overnight in a lidded alumina crucible. The resulting powder had a hint of yellow and kept afloat in deionized water. To get rid of unreacted melamine with unwanted impurities, we refluxed the suspension for three hours. The final white powder was collected by centrifugation, followed by filtration, and then it was dried at ambient temperature.

#### *Synthesis of Melem hydrazine (MH)*

The MH of monomeric unit, from 2, 5, 8 – trihydrazino – s – heptazine, is the result of the hydrothermal method's reaction between melem and hydrazine hydrate with a small modification from a reported study. In brief, 3.2 g of melem was mixed with 30 mL of 60% hydrazine hydrate aqueous solution and then placed within an autoclave walled with titanium foil. We heated the autoclave at 140 °C for 24 h. After cooling, we added 50% HCl to the resultant yellowish solution suspension to maintain a pH of between 1–2. Next, the mixture was decanted in a 100 ml beaker. Filtration was used to get rid of the unreacted solid residue that contained melem. To precipitate it, a 50% NaOH solution was added to the filtrate of pH between 7.5 and 8.5. The resulting precipitate was collected and to remove further impurities HCl was added and dissolved the precipitate. Then it was filtered, and NaOH was added again to precipitate. This procedure was repeated three times. The resultant item was vacuum-dried after being repeatedly rinsed with DI water and ethanol.

#### *Synthesis of *g*-C<sub>3</sub>N<sub>5</sub> – Polymer*

Melem hydrazine was heated to 450 °C at a heating rate of 2 °C/min and maintained at that temperature for two hours in order to create a *g*-C<sub>3</sub>N<sub>5</sub> polymer. The obtained orange powder was utilized in the further process [27].

### 2.2.3 Synthesis of the ZnO/*g*-C<sub>3</sub>N<sub>5</sub> photocatalyst

In a glass beaker with 20 mL of deionized water, 0.1256 g of *g*-C<sub>3</sub>N<sub>5</sub> was added. After that, the mixture

was sonicated for 30 min. The reaction mixture in the beaker was then stirred for 22 h using a magnetic stirrer with 0.05 g of ZnO added. The precipitates were then repeatedly filtered and washed with de-ionized water and ethanol. After that, the material was dried in a hot air oven at 80 °C for 8 h. The obtained powder was calcinated for 4 h at 450 °C, heating at a rate of 3 °C/min, to produce ZnO/*g*-C<sub>3</sub>N<sub>5</sub>.

## 2.3 Characterization

The confirmation of the nanoparticle formation by Powder X-Ray Diffraction (PXRD). The UV-visible absorption spectrometer was used to collect the UV-visible spectrum. The data from Fourier Transform Infrared Spectroscopy were collected in the 500–4000 cm<sup>-1</sup> range. Scanning electron microscopy (SEM) has been utilized to know the morphology of samples. The higher resolution–transmission electron micro spectrum (HR–TEM) was used for the microscopic investigations. X-ray Photoelectron Spectroscopy measurements were utilized for the oxidation states of the elements. During the data collecting process, charge correction was provided by the electron flood cannon. Moreover, using C1s at 284.6 eV as the standard peak, each core-level spectrum was examined for charge and adjusted as necessary. Using Casa XPS software, the experimental peaks were fitted using a combination of Gaussian and Lorentzian peaks following the Shirley background subtraction process.

The electrochemical applications were performed by electrochemical analyzer [CH Instruments] having electrochemical cell measured 10 mL of standard three electrode configurations maintained at room temperature. The functioning electrode was made by a glassy carbon electrode (GCE) modified with a thin film of ZnO/*g*-C<sub>3</sub>N<sub>5</sub>, a Pt wire functioning as a counter electrode, and the third electrode is Ag/AgCl (3M KCl) which is a reference electrode. Nitrogen gas will be used to degas the solution to make it ultrapure of about 10 mins to remove left dissolved oxygen before the analysis. The pH was maintained and analyzed during the experiment.

## 2.4 Activity testing

### 2.4.1 Rhodamine B degradation

The photocatalytic experiment was performed utilizing a 125W mercury vapor lamp as a light source

in a round glass reactor with a 176.6 cm<sup>2</sup> surface area at room temperature. In an open-air condition, the reaction mixture is placed 25 cm away from the light source and is exposed directly. For photocatalytic experiments, double-distilled water is utilized. In this experiment optimized 10 mg of ZnO/g-C<sub>3</sub>N<sub>5</sub> was dispersed in 100 mL of 10 ppm Rhodamine B (RhB) solution. The reaction mixture was shaken for half an hour before the photocatalytic experiment to establish adsorption and the balance of desorption.  $Q = (C_0 - C) V / W$ , where W is the weight of the catalyst used, V is the volume of the reaction mixture, C<sub>0</sub> & C are the concentrations of solution before and after the degradation, and Q is the extent of degradation, was used to calculate the extent of degradation. 5 mL of the reaction mixture were collected at predetermined intervals of 15 minutes, and after centrifuging to eliminate any remaining catalyst particles, the absorbance was assessed by a spectrophotometer to identify the concentration of dye.

#### 2.4.2 Mercury detection

##### Preparation of ZnO/g-C<sub>3</sub>N<sub>5</sub> modified GCE

GCE is utilized as a conducting substrate for sensor applications. Before being changed, the GCE was sonicated for 10 minutes after being polished with an alumina slurry that had 1.0, 0.3, and 0.05 μm alumina particles that were cleaned with double-distilled water all the time. The sensor electrode was developed by physically drop casting 10 μL of an aqueous colloidal dispersion of ZnO/g-C<sub>3</sub>N<sub>5</sub> (1 mg mL<sup>-1</sup>) over the pretreatment GCE. It was then allowed to dry at room temperature (27 ± 2 °C) before being exposed to electrochemical measurement.

##### Analytical procedure

CV was recorded in 3 electrode configurations dipped in an acetate buffer solution of pH 4 with and without mercury in the potential window from -0.2 to 0.5 V keeping a constant scan rate of 50 mV/Sec. Differential pulse anodic stripping voltammetry (DPASV) was analyzed in the same electrochemical cell of the same potential range with 0.05 s for the pulse width and 0.01 V for the amplitude. A measured quantity of Hg was added to the cell containing an acetate buffer. The solution was stirred with the help of a magnetic stirrer in a controlled way. The solution was stirred for 3 min continuously in the presence of

the fabricated electrode. The resulting readings were recorded.

### 3 Results and Discussion

#### 3.1. Characterization of synthesized ZnO/g-C<sub>3</sub>N<sub>5</sub>

According to PXRD patterns seen in Figure 2(a), the phase and composition of the samples ZnO/g-C<sub>3</sub>N<sub>5</sub>, ZnO and g-C<sub>3</sub>N<sub>5</sub> were identified. The asterisk (\*) denotes the corresponding approximate peak positions of the characteristic peaks (100) and (641) of g-C<sub>3</sub>N<sub>5</sub>, which correspond to the layered graphite-like structures and one triazole and two triazine moieties in the plane at 13.23 and 27.08 [28]. The visible light sensitivity, band gap, and separation of photogenerated electrons and holes are all improved in g-C<sub>3</sub>N<sub>5</sub> due to triazole moiety, which has pyrrolic N sites and more electrons than triazine, which enhances its basic catalytic activity [29]. As illustrated in Figure 2(a), bare ZnO displays the fundamental peaks at 31.85, 34.57, 36.33, 47.68, 56.74, 62.98, 66.53, 68.08, 69.24 and 77.14, which are ascribable to the planes' respective diffractions of (100), (002), (101), (102), (110), (103), (200), (112), (201), and (202) (as per JCPDS Card No. 36-1451) [21] and double diffraction peaks belonging to g-C<sub>3</sub>N<sub>5</sub>, 13.23 and 27.08 corresponding to (100) and (641) planes can be well characterized (as per JCPDS Card No. 87-1526). In addition, the ZnO/g-C<sub>3</sub>N<sub>5</sub> composite displays a sequence of peaks for diffraction at 2θ of 13.23, 27.08, 31.85, 34.57, 36.33, 47.68, 56.74, 62.98, 66.53, 68.08, 69.24 and 77.14 corresponding to (100), (641), (100), (002), (101), (102), (110), (103), (200), (112), (201) and (202) planes respectively.

PXRD data was further employed as a tool to determine the average size of crystallites through the application of Scherrer's formula, which is given in Equation (1).

$$D = \frac{0.9\lambda}{\beta \cos\theta} \quad (1)$$

where β is the greatest intensity peak-derived full width half-wave maximum (FWHM), whose 2θ values are 31.8, 34.4, 36.3, 47.5, 56.6, 62.9 and 68.0 for ZnO/g-C<sub>3</sub>N<sub>5</sub>, and 34.2, 38.1, 47.8, 56.4, 62.1, and 68.7 for ZnO nanoparticles, λ is the X-ray wavelength, whose value is 0.15406nm and the Bragg's angle is θ. The dislocation density, δ has been calculated by the formulae (Equation (2)).

$$\text{Dislocation Density, } \delta = \frac{1}{D^2} \quad (2)$$

Where, D is the size of the crystallite.

The stress has been determined using the formula (Equation (3)),

$$\text{Stress} = \frac{\text{Microstrain} \times E}{2} \quad (3)$$

Where, E is Young's Modulus for a particular material, for ZnO it is found to be 140GPa and for g-C<sub>3</sub>N<sub>5</sub> it is found to be 194GPa. Microstrain ( $\epsilon$ ) =  $\beta/(4\text{tan}\theta)$ , where the maximum intensity peaks are used to determine the full width half-wave maximum (FWHM), denoted by  $\beta$ , and  $2\theta$  is the peak position.

The computed mean dislocation densities, stress factors, and crystallite sizes for the synthesized samples are displayed in Table 1. It was discovered that the ZnO/g-C<sub>3</sub>N<sub>5</sub> nanocomposite's average crystallite size was found to decrease when compared to the nanoparticle ZnO. The reduced grain size will undoubtedly produce an increased specific surface area, which can raise the photocatalytic reaction rate. Any crystal's dislocation density of a material is the measure of its dislocation lines per volume unit [30]. It describes the topological flaws in a crystal structure that dictate the many characteristics of that substance [31]. The more substantial value of dislocation density suggests a higher degree of material hardness because the movement of one dislocation is impeded by the other dislocations present. In this instance, ZnO/g-C<sub>3</sub>N<sub>5</sub> possesses a higher dislocation density.

**Table 1:** Calculated crystallite size from Scherrer's formula, dislocation density and stress of ZnO and ZnO/g-C<sub>3</sub>N<sub>5</sub>.

Samples	Crystallite size D (nm)	Dislocation density $\delta$ (nm <sup>-2</sup> )	Stress ( $\epsilon$ ) $\times 10^{-3}$
ZnO/g-C <sub>3</sub> N <sub>5</sub>	21	2.7	4.4
ZnO	26	1.8	3.3

The DRS and absorbance studies have been used to investigate the optical characteristics. For ZnO, g-C<sub>3</sub>N<sub>5</sub>, and ZnO/g-C<sub>3</sub>N<sub>5</sub>, the absorbance spectra were acquired (Figure 2(b)). Even though all of the samples' absorbance edges are in the visual range, ZnO's absorbance edge is relatively lower than those of the other samples. It is interesting to see that the absorbance edge moved towards the higher end with the composite mixture containing g-C<sub>3</sub>N<sub>5</sub>. It was reported that the ZnO/g-C<sub>3</sub>N<sub>5</sub> sample exhibited

increased visible light absorption due to a fall in the energy bandgap value of ZnO from 3.08 eV to ZnO/g-C<sub>3</sub>N<sub>5</sub> 2.74 eV. From the absorbance spectra, the bandgap was determined (Figure 2(c)), which was recorded in the range 200–800 nm. Interestingly, ZnO/g-C<sub>3</sub>N<sub>5</sub> yielded the lower bandgap value of 2.74 eV. Therefore, it is possible to verify the likelihood of this system developing into a better photocatalyst.

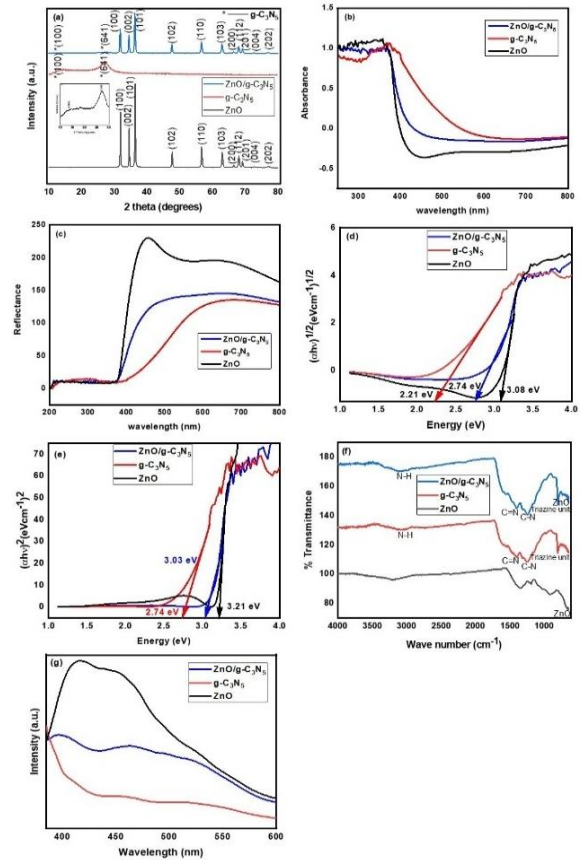


**Figure 2:** (a) PXRD patterns, (b) UV-visible absorbance spectra, (c) UV-visible DRS, (d) energy gap spectra  $(\alpha h\nu)^{1/2}(\text{eVcm}^{-1})^{1/2}$ , (e) energy gap spectra  $(\alpha h\nu)^2(\text{eVcm}^{-1})^2$  (f) FTIR spectra and (g) PL spectra of ZnO/g-C<sub>3</sub>N<sub>5</sub>, g-C<sub>3</sub>N<sub>5</sub> and ZnO samples.

The bandgap width of the synthesized heterojunction nanocomposites was calculated by Tauc's plot formula (Equations (4) and (5)), and the respective  $E_g$  is presented in Figure 2(d) and (e).

$$\alpha h\nu = A (h\nu - E_g)^{1/2} \quad (4)$$

$$\alpha h\nu = A (h\nu - E_g)^2 \quad (5)$$

where  $\alpha$  is the absorbance of the sample,  $A$  is the index of refraction,  $h\nu$  is the incident energy of the photon,  $E_g$  is the optical bandgap energy.

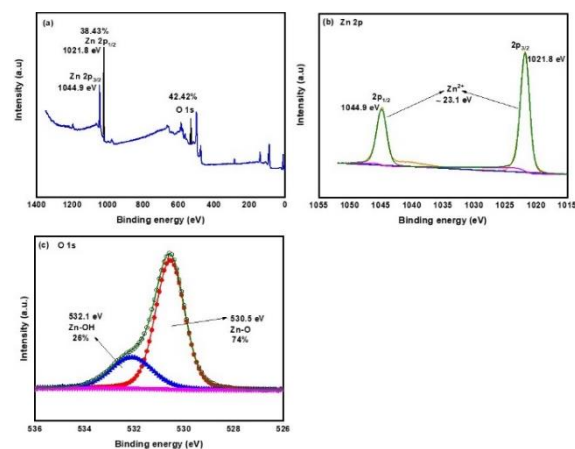
Using the Tauc method, the photocatalyst samples' bandgap energy was determined, and the optical bandgap of ZnO, g-C<sub>3</sub>N<sub>5</sub> and ZnO/g-C<sub>3</sub>N<sub>5</sub> samples were determined from the plot of indirect allowed transitions  $(\alpha h\nu)^{1/2}$  comparing  $h\nu$  (Figure 2(d)). Approximately 3.08 eV, 2.21 eV, and 2.74 eV were elicited, respectively. Thus, using this data, we were able to calculate the ideal bandgap value for ZnO/g-C<sub>3</sub>N<sub>5</sub>, which came out to be 2.74 eV. So we only examine this indirect allowed transitions plot. The addition of g-C<sub>3</sub>N<sub>5</sub> to ZnO modifies the electronic properties of nanocomposite ZnO/g-C<sub>3</sub>N<sub>5</sub>. This introduces additional energy levels in the bandgap, resulting in modifications to the bandgap energy. The ZnO/g-C<sub>3</sub>N<sub>5</sub> sample's estimated bandgap energy is significantly lower than that of pure ZnO, as seen in Figure 2(d), indicating that these nanocomposites absorb visible light efficiently. The direct allowed transitions energy bandgap spectra of ZnO, g-C<sub>3</sub>N<sub>5</sub>, and ZnO/g-C<sub>3</sub>N<sub>5</sub> are shown in Figure 2(e). They were found to be 3.21 eV, 2.74 eV, and 3.03 eV, respectively.

Figure 2(f) shows the FT-IR spectrum of ZnO, g-C<sub>3</sub>N<sub>5</sub>, and ZnO/g-C<sub>3</sub>N<sub>5</sub>. ZnO was confirmed to be present in the composite by the observation of the characteristic absorption peak of the ZnO in ZnO/g-C<sub>3</sub>N<sub>5</sub>. Most importantly, the peak at 655 cm<sup>-1</sup> was identified as the Zn-O stretching vibration in distinct ZnO samples [32]. A band at 1380–1500 cm<sup>-1</sup> may arise from C-O or C-H bending vibrations, especially if the ZnO sample contains organic compounds or carbonate contamination from adsorbed CO<sub>2</sub> [33]. The intensity of the peak at 3070 cm<sup>-1</sup> is linked to the stretching vibration absorption peak of the -NH<sub>2</sub> [34]. Two triazole ring stretching and deformation modes that are heavily copulated are associated with the peak at 1680–1690 cm<sup>-1</sup> [35]. The peak at 1422 cm<sup>-1</sup> is associated with the stretching vibration peak of the triazole nucleus ring. The stretching vibration peak of the C-N bonding is responsible for the absorption that ranges from 1300 cm<sup>-1</sup> to 1270 cm<sup>-1</sup>. The absorption is ascribed to N-H bending vibrations between 700 and 1000 cm<sup>-1</sup> [36].

Electrons in the VB are stimulated to the CB when semiconductors are exposed to light, creating electron-hole pairs. Nevertheless, these charge carriers tend to quickly recombine and eventually be destroyed if they are not used efficiently. For semiconductors to attain improved photocatalytic activity under light

irradiation, photogenerated electrons and holes must be effectively separated. Since PL is an established method for describing the recombination efficiency of photogenerated electron-hole pairs, 325 nm excitation wavelengths were used to measure emission spectra at room temperature (Figure 2(g)). ZnO/g-C<sub>3</sub>N<sub>5</sub> exhibits two emission peaks at 395 and 460 nm, that represent the properties of ZnO and g-C<sub>3</sub>N<sub>5</sub>, respectively. ZnO/g-C<sub>3</sub>N<sub>5</sub> exhibits a redshifted and decreased fluorescence emission intensity in comparison to ZnO. This finding suggests that there is delayed photoelectron-hole recombination. Furthermore, the presence of the red shift indicates that ZnO and g-C<sub>3</sub>N<sub>5</sub> form a heterojunction rather than merely being physically combined. By successfully aiding in the separation of photogenerated carriers, the heterojunction creation greatly increases photocatalytic activity of ZnO/g-C<sub>3</sub>N<sub>5</sub>.

The ZnO nanoparticles formed are analyzed by XPS and depicted in Figure 3. The XPS survey spectrum is shown in Figure 3(a) where Zn and O peaks are visible. Figure 3(b) demonstrates the Zn 2p region's high resolution XPS spectrum. The two peaks in the Zn 2p core-level area seen in Figure 3(b) were ascribed to Zn 2p<sub>1/2</sub> and Zn 2p<sub>3/2</sub>, and are roughly located at 1021.8 eV and 1044.9 eV, correspondingly, with a binding energy difference of 23.1 eV.



**Figure 3:** (a) wide scan spectrum of ZnO nanoparticles (b) narrow scan spectra of Zn and (c) narrow scan spectra of O.

This indicated the existence of Zn in the +2 oxidation state on the surface of the nanoparticle [37], [38]. Figure 3(c) displays the core level spectra of O in ZnO. As shown in Figure 3(c), O exists in two different oxidation states. The lower peak, positioned

near binding energy 530.5 eV allocated to the -2 oxidation state in ZnO [39]. The second peak, which is situated at 532.1 eV, results from the OH group being absorbed into the ZnO nanoparticles' surface [40].

The synthesized g-C<sub>3</sub>N<sub>5</sub>'s XPS spectra, as reported by Liu *et al.*, are shown in Figure 4(a) and have unique peaks [41] for the composition, which consists of two units of s-heptazine connected by an azo bond. The survey spectra revealed that the peaks C and N contain a trace quantity of O. The N 1s core level spectra in Figure 4(b) are resolved into two components. N in C=N-C is responsible for the peak at 398.6 eV, and N=N and N-CH<sub>2</sub> in the molecule are responsible for the peak at 400.1 eV [30]. In C 1s core level spectra Figure 4(c), the peaks resolved into 284.8 eV, and 287.9 eV are ascribed to adventitious Carbon (C-C), and the sp<sup>2</sup> hybridized carbon atom bonded to N as (N-C=N-) respectively [42]. Theoretical XPS elemental analysis at%, observed (theoretical): N-63.26 (62.54), C-36.79 (37.53), empirical formula: C<sub>3</sub>N<sub>5.19</sub> (C<sub>3</sub>N<sub>5</sub>), N<sub>ring</sub>: N<sub>bridging</sub> at%, and theoretical atomic ratio: 60.45: 39.64 and ~3:2, (60:40, 3:2).

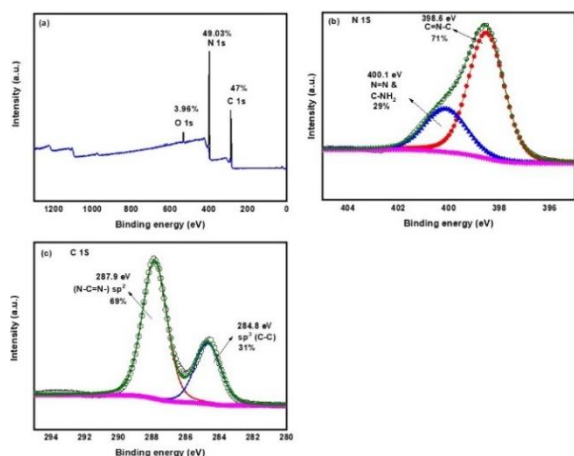


**Figure 4:** (a) wide scan spectrum of g-C<sub>3</sub>N<sub>5</sub> (b) narrow scan N 1s spectra and (c) narrow scan C 1s spectra.

The XPS spectrum data for the g-C<sub>3</sub>N<sub>5</sub>/ZnO composites are shown in Figure 5. As expected, Zn is present in the survey spectrum Figure 5(a) along with C, N, and O. The N 1s peaks in the HR scan Figure 5(b) could be separated into two primary peaks: 399.5 eV from N=N and C-NH<sub>2</sub> from azo and tertiary N atoms and 398.6 eV representing C=N-C from the triazine ring. Three peaks, 284.6 eV, 286.1 eV, and 288.0 eV adventitious C (C-C), C-O, and -C=N, respectively, were identified in the C 1s spectra Figure 5(c). The high-resolution spectra of O 1s are shown in Figure 5(d).

On the composite surface, O<sub>2</sub> ions in Zn-O partially bound to C- (Zn-O-C) coincide with the peak at 531.3 eV. The peaks at 1044.9 and 1021.1 eV in the Zn 2p spectra Figure 5(e) corresponded to Zn 2p<sub>1/2</sub> and Zn 2p<sub>3/2</sub>, respectively, which stand for typical Zn<sup>2+</sup> ions. ZnO and g-C<sub>3</sub>N<sub>5</sub> were shown to be associated, according to the XPS study.

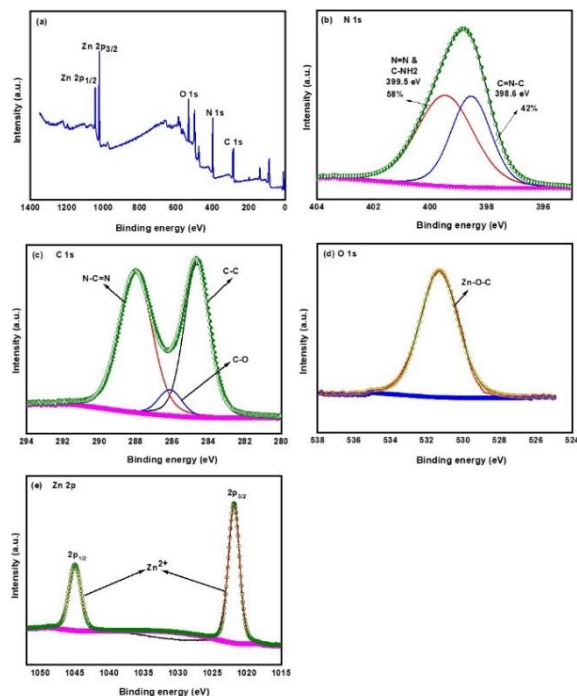


**Figure 5:** (a) wide scan spectrum of g-C<sub>3</sub>N<sub>5</sub>/ ZnO, narrow scan (b) N 1s (c) C 1s (d) O 1s (e) Zn 2p spectra.

The surface morphology and microstructure of the g-C<sub>3</sub>N<sub>5</sub>, ZnO, and ZnO/g-C<sub>3</sub>N<sub>5</sub> nanocomposites were assessed using FE-SEM, as illustrated in Figure 6(a)–(f). As shown in Figure 6(a)–(b), the rod-like and layered sheet structure of g-C<sub>3</sub>N<sub>5</sub> is favorable for ZnO attachment onto g-C<sub>3</sub>N<sub>5</sub> surface [43]. On the other hand, Figure 6(c)–(d) of the SEM analysis of ZnO reveals a higher number of uneven, agglomerated, spongy holes and voids [44]. Interestingly, ZnO/g-C<sub>3</sub>N<sub>5</sub> electron microscopic images show that even after merging, the structure of the individual components remains unchanged. The nanorod-like crystal structure of g-C<sub>3</sub>N<sub>5</sub> is covered with the spongy, aggregated ZnO, which is clearly visible in Figure 6(e)–(f). In addition to the XRD data, SEM images provide additional proof that composites were successfully created [45]. When we compare the

average particle diameter in Fig. 7a with the SEM and TEM data, and then with the XRD data, it is well matched. Which ranges from 22 to 46 nm with an average diameter of about 34 nm, is determined by the ImageJ computer software. The respective EDS spectra are displayed in Figure 7(b), which indicates that the ZnO/g-C<sub>3</sub>N<sub>5</sub> sample contains the components Zn, C, O and N. (The Cu appearance is due to the copper grid during the sample analysis).

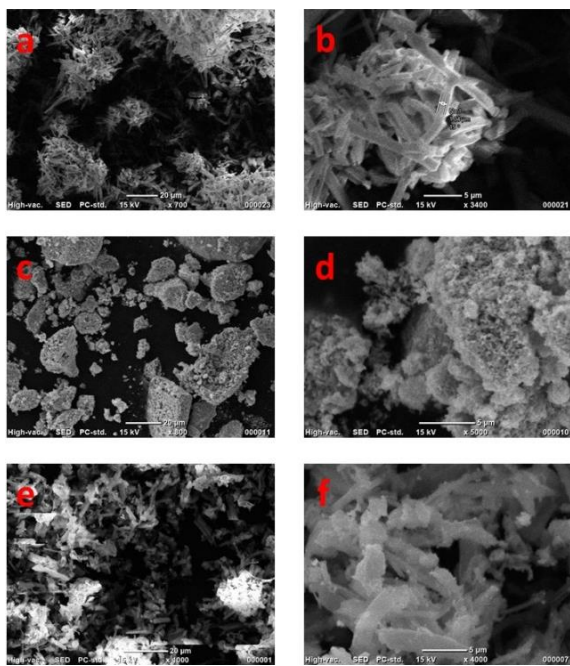


**Figure 6:** SEM Images of (a)–(b) g-C<sub>3</sub>N<sub>5</sub>, (c)–(d) ZnO and (e)–(f) ZnO/g-C<sub>3</sub>N<sub>5</sub>.

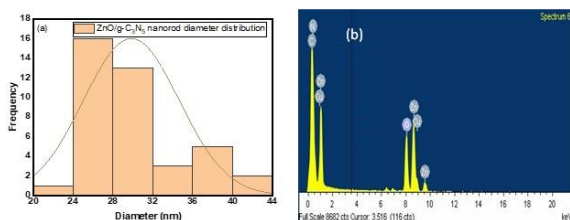


**Figure 7:** (a) Gaussian distribution and (b) EDS spectra of ZnO/g-C<sub>3</sub>N<sub>5</sub> NCs.

TEM was used to inspect the dispersivity, shape, and size of the particles. The representative TEM micrograph of the ZnO/g-C<sub>3</sub>N<sub>5</sub> sample is presented in Figure 8(a). The TEM data revealed the ZnO/g-C<sub>3</sub>N<sub>5</sub> NPs spherical shape. The image computer program measured the particle diameter of the NPs, which varies from 25.74 to 45.57 nm with an average

diameter of 34.91 nm, and their respective histogram is given in Figure 8(b), which is well matched with XRD data of average crystallite particle size. Furthermore, utilizing the TEM micrograph, we were able to capture a ZnO/g-C<sub>3</sub>N<sub>5</sub> NP crystal lattice (Figure 8(c)). The magnitude of the crystal lattice distance was calculated to be 0.24 nm. The ZnO/g-C<sub>3</sub>N<sub>5</sub> lattice's d-spacing in the (100) plane was validated by the captured lattice distance (JCPDS file no. 361451). The ZnO/g-C<sub>3</sub>N<sub>5</sub> NP's crystalline nature and high purity have been confirmed by these results. To corroborate the preceding results even more, selected area electron diffraction (SAED) was also carried out; the resulting pattern is displayed in Figure 8(d). The electron diffraction ring's interplanar distance was precisely measured, and the results indicate that the rings are composed of a ZnO/g-C<sub>3</sub>N<sub>5</sub> phase. JCPDS file no. 361451 contains the measured d-spacing values that have been allocated to the respective crystal planes.

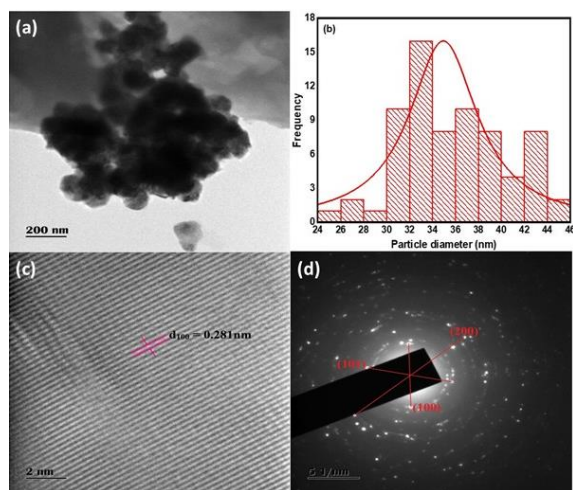


**Figure 8:** (a)TEM, (b) Gaussian curve, (c) HRTEM and (d) SAED pattern images of ZnO/g-C<sub>3</sub>N<sub>5</sub> NCs.

### 3.2. Photocatalytic degradation

A semiconductor photocatalyst's assistance in the photocatalytic degradation process is dependent on many factors, including pH, light source and intensity, organic substrate type and concentration, semiconductor photocatalyst concentration and type, and others. The absorption of the Rhodamine B dye was measured for ZnO/g-C<sub>3</sub>N<sub>5</sub> and ZnO using a UV-visible spectrophotometer, Figure 9(a)–(b) and Figure 9(c) show the degradation percentage over time.

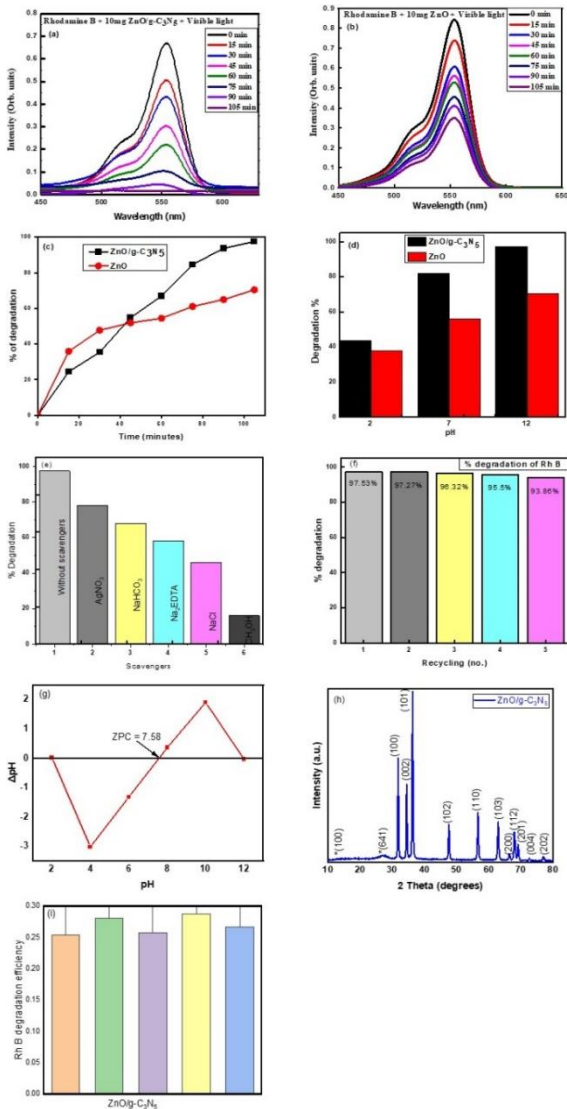


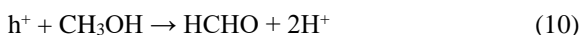
**Figure 9:** (a) Rhodamine B dye absorbance spectra in visible light for ZnO/g-C<sub>3</sub>N<sub>5</sub>, (b) Rhodamine B dye absorbance spectrum in visible light for ZnO, (c) Plot showing the percentage of RhB degradation under visible light, (d) effects of pH variation on Rhodamine B degradation by heterogeneous photocatalysis using ZnO/g-C<sub>3</sub>N<sub>5</sub>, (e) impact of radical scavengers on degradation of RhB on ZnO/g-C<sub>3</sub>N<sub>5</sub> in visible light, (f) ZnO/g-C<sub>3</sub>N<sub>5</sub> photocatalyst's capacity to be recycled for the decolorization of RhB in visible light, (g) point of zero charge measurement for ZnO/g-C<sub>3</sub>N<sub>5</sub> by pH drift method, (h) XRD pattern of the catalyst after degradation studies and (i) Rh B degradation efficiency error bars.

The pH effect on dye degradation was studied at varying concentrations of HCl and NaOH. The maximum degradation percentage was measured at pH 12 and declined at pH levels that were both neutral and acidic (Figure 9(d)). In addition to influencing ZnO/g-C<sub>3</sub>N<sub>5</sub>'s surface characteristics, pH also has an impact on dye molecule dissociation and free radical production. Because the generated free radicals also impact the deterioration process, a decrease in pH from the baseline value lowers the degradation percentage. Although we attempted to achieve a high degrading efficiency of 97.53% at basic pH, it worked well in situations with severely acidic (44%) and neutral (82%) pH levels.

Rh B concentration varied from 2 ppm to 20 ppm while ZnO/g-C<sub>3</sub>N<sub>5</sub> (10 mg/100 ml) was kept constant. This allowed researchers to examine the impact of the starting Rh B concentration on the degrading efficiency. An increase in the initial dye concentration was observed to lower Rh B's breakdown efficiency. For the degradation to occur, the catalyst's active surface that is available for the reaction is essential, however, when the dye concentration rises from 2 ppm to 10 ppm and there is a constant catalyst quantity (10 mg/100 mL), this results in increased active sites, 10 ppm to 15 ppm, results in constant active sites, and 15 ppm onwards, reduces the number of active sites in the reaction. When dye molecules are multiplied, the mixture becomes more intensely colored and the light intensity of photons that pass into the solution is decreased; so, only merged photons will reach the surface of the catalyst. Therefore, the evolution of hydroxyl and superoxide radicals was limited. Further increases the concentration of the dye, the light intensity is reduced and photodegradation was found to be negligible. In the ZnO/g-C<sub>3</sub>N<sub>5</sub> tests, several dosages of 5, 10, 20, 30, 40, and 50 mg were employed while keeping the dye concentration constant at 10 ppm. It was found that the decrease in Rh B degradation efficiency with an increase in catalyst quantity could be due to a decrease in light penetration from turbidity. At a minimum of 10 mg of catalyst, we were able to get excellent degradation. Next, we set the dye concentration at 10 ppm and the catalyst dosage at 10 mg.

Additionally, as shown in Figure 9(e), scavenging tests were also conducted with the same 10 ppm dye concentration to confirm if extremely potent free radicals could cause Rh B dye to photodecolorize while exposed to visible light and with a ZnO/g-C<sub>3</sub>N<sub>5</sub> photocatalyst. Five distinct scavengers are used for the photo decolorization experiment. Under visible light,

the scavenger's effect has performed using AgNO<sub>3</sub>, NaHCO<sub>3</sub>, Na<sub>2</sub>EDTA, NaCl and CH<sub>3</sub>OH reveals 78%, 68%, 58%, 46% and 16% for Rh B, respectively. The possible mechanism for scavengers is given in the following Equations (6)–(10) [5], [50], [51]:



These data suggested that OH<sup>•</sup> (radicals) and h<sup>+</sup> (holes) are involved in the degradation of Rh B dye [52]. Five replications of ZnO/g-C<sub>3</sub>N<sub>5</sub> NC were examined for repeatability. Before being utilized again in the following photocatalytic experiment, the ZnO/g-C<sub>3</sub>N<sub>5</sub> employed in the photocatalytic treatment was filtered and dried at 30 to 40 °C in a hot air oven. It was noticed that for the first cycle, the percentage degradation was 97.53%, in the second cycle the percentage degradation was 97.27%, then for the third cycle 96.32%, for the fourth and fifth cycles it was about 95.5 and 93.86% respectively. The trend has decreased due to the loss of some NC particles during the filtration. After repeated use, there is very little change in the photodegradation efficiency of ZnO/g-C<sub>3</sub>N<sub>5</sub>. (Figure 9(f)) suggesting it is the best catalysts for reusability also cost-effective. A comparison of degradation efficiency for Rhodamine B with different catalysts is given in Table 2. Compared to other catalysts, the synthesized ZnO/g-C<sub>3</sub>N<sub>5</sub> combination showed superior degradation. Figure 9(a) displays the maximum amplitude of absorbance that can occur at 554 nm, and it gradually decreases with reaction time. Deterioration as a percentage is 97.53%. This work demonstrates unequivocally that the ZnO/g-C<sub>3</sub>N<sub>5</sub> nanocomposite is a powerful catalyst for the degradation of the dye rhodamine B.

To understand the surface properties, pH drift method was employed to identify pHPZC (point of zero charge), which is the pH at which the charge on the surface of the adsorbent is zero. 50 mL of 0.01 N NaCl was added to a series of conical flasks. The pH initial for the series of solutions was adjusted from 2 to 12 by adding 0.01 N HCl and 0.01 N NaOH. Once pH initially attained a constant value, 0.01 g of adsorbent was added to each conical flask and closed tightly.

Then the solutions were stirred continuously for 12 hours to attain equilibrium. pH of the solution measured after attaining equilibrium was considered as pH final. The point at which pH(initial) = pH(final) is called the pHPZC for the adsorbent. The pHPZC of ZnO/g-C<sub>3</sub>N<sub>5</sub> is found to be 7.58 as shown in Figure 9(g). This implies that below this pH, the surface of the adsorbent becomes positively charged due to the protonation which would prefer the adsorption of anionic species. Above pHPZC of 7.58, the surface of the nanocomposite intends to be negatively charged which can be sustained by -OH groups. This explains the potential of the adsorbent to facilitate the adsorption of cationic moieties. Following the degradation studies, the material stability was displayed in Figure 9(h), which demonstrates that the catalyst's structural deterioration is not significantly different and that all of the assigned peaks are visible after five cycles, proving the material stability.

Information about the kinetic analysis of ZnO and ZnO/g-C<sub>3</sub>N<sub>5</sub> photocatalysts under visible light is given in Table 3. This indicates that the rate is 0.0124 min<sup>-1</sup> for ZnO and 0.0274 min<sup>-1</sup> for ZnO/g-C<sub>3</sub>N<sub>5</sub>. Compared to ZnO, ZnO/g-C<sub>3</sub>N<sub>5</sub> shows a fluorescence emission intensity reduced at 395 nm and 460 nm (Figure 2(f)). This result implies that photoelectron-hole recombination is delayed, which helps to achieve a very high degradation percentage for rhodamine B dye up to 97.53%. Additionally, we attempted to determine the percentage of rhodamine B degradation using a commercially available TiO<sub>2</sub>/P<sub>25</sub> catalyst, and we were able to get up to 93.21% degradation [53]. We can therefore conclude from this comparison that our catalyst performs better than this. Furthermore, we have included the rhodamine b degrading efficiency error bars after executing numerous trials repetitively (Figure 9(i)).

**Table 2:** Comparison of Rh B dye degradation with other catalysts.

Photocatalyst	Light utilized	Time (min)	Degradation %	Ref.
WO <sub>3</sub> /TiO <sub>2</sub>	Visible light	80	95.31%	[46]
g-C <sub>3</sub> N <sub>4</sub> /TiO <sub>2</sub>	Visible light	-	35.24%	[47]
WO <sub>3</sub> /TiO <sub>2</sub>	UV light	120	96.49%	[48]
H <sub>2</sub> O <sub>2</sub>	UV light	-	73%	[49]
ZnO/g-C <sub>3</sub> N <sub>5</sub>	Visible light	105	97.53%	This work

**Table 3:** Kinetic investigations with ZnO and ZnO/g-C<sub>3</sub>N<sub>5</sub> nanocomposite photocatalysts in visible light.

No.	Photocatalysts	Degradation %	K × 10 <sup>-3</sup> (min <sup>-1</sup> )
1	ZnO	70.39%	0.0124
2	ZnO/g-C <sub>3</sub> N <sub>5</sub>	97.53%	0.0274

### 3.3. Examining the potential mechanism of photocatalytic degradation

Based on the UV-visible DRS spectrum study, the evaluated  $E_g$  value for ZnO is 3.2 eV and g-C<sub>3</sub>N<sub>5</sub> is 2.4 eV, respectively.  $E_{VB}$ s for ZnO-2.89 eV and g-C<sub>3</sub>N<sub>5</sub> - 1.29 eV were determined by calculating the results of Eqs. (11&12).

$$E_{VB} = X - E_e + 0.5 E_g \quad (11)$$

$$E_g = E_{VB} - E_{CB} \quad (12)$$

Where,  $E_{VB}$  is energy at the valance band,  $E_{CB}$  is energy at the conduction band,  $E_g$  is band gap energy of ZnO and g-C<sub>3</sub>N<sub>5</sub>, X is the absolute electronegativity of ZnO and g-C<sub>3</sub>N<sub>5</sub> and  $E_e$  is the energy of free electrons on the hydrogen scale (~4.5eV).

The RhB photocatalytic degradation S-scheme mechanism is inferred based on the aforesaid result, as seen in Figure 10. Compared to ZnO, g-C<sub>3</sub>N<sub>5</sub> exhibits greater negative  $E_{VB}$  and  $E_{CB}$ . When exposed to visible light, the  $e^-$  from VB would migrate to CB, causing an equal number of holes to accumulate on VB. Through band bending and van der Waals forces, the  $h^+$  on the VB of g-C<sub>3</sub>N<sub>5</sub> recombine with  $e^-$  on the CB of ZnO. Both g-C<sub>3</sub>N<sub>5</sub>'s CB and ZnO's VB retain a significant amount of  $e^-$  with strong reducing and oxidizing abilities, respectively.

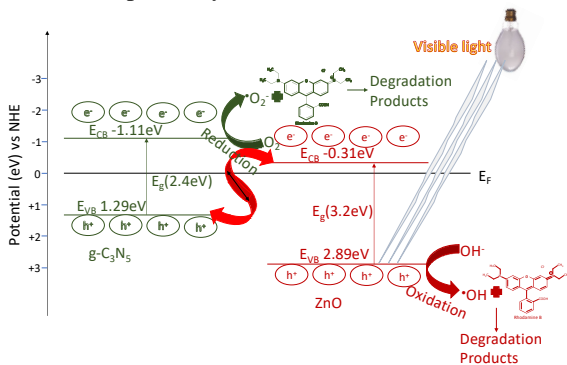


**Figure 10:** The possible photocatalytic mechanism of ZnO/g-C<sub>3</sub>N<sub>5</sub> nano-composite for the degradation of Rh B dye under visible light conditions.

O<sub>2</sub> will be reduced to the active group O<sub>2</sub><sup>•-</sup> if a lot of electrons build up on the g-C<sub>3</sub>N<sub>5</sub> CB since its CB potential is lower than the O<sub>2</sub>/O<sub>2</sub><sup>•-</sup> standard hydrogen electrode potential (-0.33 eV). Compared to the normal Potential of the hydrogen electrode for H<sub>2</sub>O/OH<sup>-</sup> (1.99 eV), the ZnO VB potential is more positive. Strong oxidation-capable holes on ZnO's VB will convert H<sub>2</sub>O to OH<sup>-</sup>, and the  $e^-$  and  $h^+$  that are

separated can effectively encourage the production of active groups like O<sub>2</sub><sup>•-</sup> and OH<sup>-</sup> [54]–[59]. Rh B would interact with the produced active groups, such as O<sub>2</sub><sup>•-</sup> and OH<sup>-</sup>, to cause its deterioration.

### 3.4. Cyclic voltammetry (CV)

#### 3.4.1 Electrochemical sensor for Hg<sup>2+</sup>

Initially, the electrochemical behavior of the ZnO/g-C<sub>3</sub>N<sub>5</sub> composite was studied by recording the cyclic voltammograms with or without Hg<sup>2+</sup> to know the interacting ability and potential affinity of the proposed composite towards mercuric ions. For better comparison, cyclic voltammograms of 10 μM of Hg<sup>2+</sup> were recorded at ZnO-modified GCE, g-C<sub>3</sub>N<sub>5</sub> modified GCE and ZnO/g-C<sub>3</sub>N<sub>5</sub> modified GCE in the range between -0.2 to 0.5 V of potential window have been measured and overlaid one above the other and is depicted in the Figure 11(a).

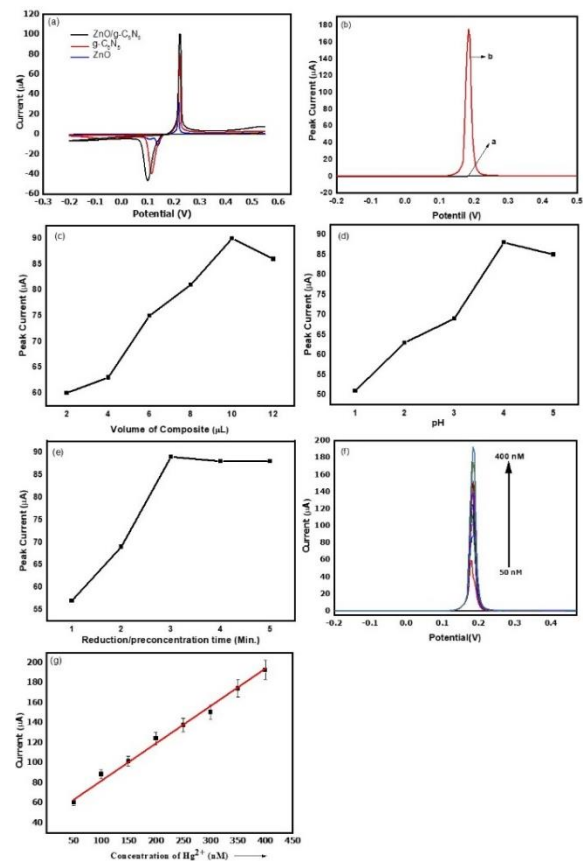


**Figure 11:** (a) Overlaid cyclic voltammetric profile of 10 μM of mercury in an acetate buffer solution of pH 4

recorded at ZnO modified GCE, g-C<sub>3</sub>N<sub>5</sub> modified GCE and ZnO/g-C<sub>3</sub>N<sub>5</sub> modified GCE in the potential window from - 0.2 to 0.5 V with a scan rate of 50 mV/Sec, (b) Differential pulse anodic stripping voltammograms recorded at ZnO/g-C<sub>3</sub>N<sub>5</sub> modified glassy carbon electrode in the absence (a) and in the presence of 400 nM of Hg<sup>2+</sup> (b) in an acetate buffer solution of pH 4. Reduction potential: 0.1 V, preconcentration time: 3 min, optimization study: (c) volume of composite, (d) pH of buffer solution and (e) Preconcentration of reduction time. The concentration of Hg<sup>2+</sup>: 100 and Reduction potential: 0.1 V, (f) Overlaid differential pulse anodic stripping voltammograms and (g) Calibration plots.

The ZnO-modified GCE showed a voltammetric peak at a peak potential of 0.13 V with a peak current of 10  $\mu$ A and in the reductive sweep which corresponds to the reduction of Hg<sup>2+</sup> to Hg<sup>0</sup> by two electrons and subsequently showed another voltammetric peak at 0.21 V with a peak current of 36  $\mu$ A in the reversal oxidative sweep which in turn corresponds to the two-electron oxidation of Hg<sup>0</sup> to Hg<sup>2+</sup>. g-C<sub>3</sub>N<sub>5</sub> modified GCE showed a reductive peak at a peak potential of 0.1 V with a peak current of 40  $\mu$ A and an oxidative peak at 0.2 V with a peak current of 81  $\mu$ A. However, the ZnO/g-C<sub>3</sub>N<sub>5</sub> modified GCE showed a reductive peak at a peak potential of 0.1 V with a peak current of 45  $\mu$ A and an oxidative peak at 0.2 V with a peak current of 100  $\mu$ A. From the above experimental voltammetric figures and data, it is very evident that, the presence of ZnO on the surface of bare GCE results in the appearance of voltammetric signature for the reduction and oxidation of mercury which may be ascribed to ZnO particles' electrocatalytic properties [60]. The voltammetric signature observed at g-C<sub>3</sub>N<sub>5</sub> is more facile than that observed at ZnO-modified GCE in terms of peak currents for both reduction and oxidation of mercury which may be due to the soft-soft interaction of soft donor atom nitrogen and soft metal mercury according to HSAB concept [61]. Surprisingly, the observation made at ZnO/g-C<sub>3</sub>N<sub>5</sub> modified GCE is superior to those observed at the ZnO and g-C<sub>3</sub>N<sub>5</sub> modified electrodes with respect to peak currents which is almost double. This, superior electrochemical behavior of the prepared composite material towards the electrochemical determination of Hg is due to the synergetic effect posed by both ZnO and g-C<sub>3</sub>N<sub>5</sub> components of the composite material. As a result of this, the interface might be employed as an alternative ion selective sensing platform for the sensitive and

selective quantification of Hg at concentrations of traces level.

From the cyclic voltammetric profile of mercury recorded at ZnO/g-C<sub>3</sub>N<sub>5</sub>, it is envisaged that the oxidation peak is more intense, and sharper than that of a corresponding reductive peak, hence the oxidative peaks were systematically studied using DPASV which in turn also helps us in order to reach the anticipated detection limits. The voltammetric stripping identification of Hg was experimented via three steps:

a) Preconcentration of Hg<sup>2+</sup> at ZnO/g-C<sub>3</sub>N<sub>5</sub> modified glassy carbon electrode at an applied reduction potential of 0.1 V for a predetermined duration of 3 min in a pH 4 acetate buffer solution with a specified concentration of Hg<sup>2+</sup> (in this step, all Hg<sup>2+</sup> ions get reduced to Hg<sup>0</sup>).

b) Reduced mercury is stripped (oxidized) and added to the electrolytic solution's bulk.

Figure 11(b) displays a typical DPASV of Hg<sup>2+</sup> (100 nM). In the absence of mercury ions, the ZnO/g-C<sub>3</sub>N<sub>5</sub> interface exhibited no voltammetric signature; nevertheless, when mercury ions were present, it displayed a distinct, sharp peak at 0.18 V, which is indicative of the oxidation (stripping) of preconcentrated Hg<sup>0</sup> on the interface's surface. According to this observation, the changed interface may have had a potential affinity for mercury, making it a suitable interface for electrochemically quantifying mercury at very low concentrations.

#### 3.4.2 Optimization parameters influencing the analytical studies

The interaction of each sensor material with the target analyte is specific and mainly depends on the experimental conditions such as thickness of the modifier, pH of buffer solution, preconcentration time (pct) and reduction potential which in turn decides maximal effectiveness of the suggested interface for measuring mercury ions in aqueous solution electrochemically in relation to the intensity of analytical signal, least detection limits and interference from foreign chemicals [62].

The preconcentration or accumulation of Hg<sup>2+</sup> on the surface of ZnO/g-C<sub>3</sub>N<sub>5</sub> composite mainly depends on the amount of composite present on the electrode surface in turn depends on the volume of composite used to make the thin film on the glassy carbon electrode [47]. The aqueous colloidal solution volume of the composite is adjusted between 4 and 12 mL while keeping the glassy carbon electrode's area



constant (Figure 11(c)). The stripping current increases from 4  $\mu\text{L}$  to 10  $\mu\text{L}$  and then after it decreases. Hence the volume of composite for all further studies is fixed as 10  $\mu\text{L}$ .

The preconcentration of metal ions from the bulk of the electrolytic solution onto the surface of the modified electrode at the interface, where the preconcentration is achieved through a particular interaction between the metal ion and the modifier molecule, is greatly influenced by the buffer solution selection. Acetate buffer solution of varying pH has been examined for the determination of mercury. Because of this, the acetate buffer solution's pH impact was examined in the pH range of 1 to 4 (Figure 11(d)). The peak current increased from 1 to 4 and then declined. The increased magnitude of the modifier-mercury ion interaction may be the cause of the peak current rise. Acetate buffer solution with a pH of 4 is utilized as an ideal pH for additional analysis when the peak current starts to decline.

Additionally, it has been investigated how long it takes for the mercury ion to preconcentrate on the surface of a modified electrode, ranging from 1 to 5 min (Figure 11(e)). For the stripping of mercury, the peak current rises for one to three minutes before falling. The longer the preconcentration period, the more analytes concentrate at the electrode/solution contact, which causes the peak current to increase. Either surface saturation or the achievement of equilibrium between the metal ions at the interface and the ions in the bulk of the solution can be blamed for the peak reduction in peak current after three minutes. As a result, three minutes has been chosen as the ideal preconcentration duration for all further research. The reduction of the mercury ion to mercury at 0.1 V has been taken straight from the cyclic voltammogram (Figure 11(f)).

### 3.4.3 Calibration and detection limit

In order to apply the developed sensor interface for real sample analysis, it is adequate to measure the concentration range wherein the interface works linearly. In this regard, as per the results from optimal conditions, the peak currents were measured by the calibrated plot for the stripping of  $\text{Hg}^{2+}$  by the successive additions of 50 nM mercury ions by solution.

A glassy carbon electrode (GC) containing multiwalled functionalized carbon nanotubes (MWCNTs) immobilized within a dihexadecyl hydrogen phosphate film (DHP) is proposed as a

nanostructured platform for determination of mercury (Hg) concentration using differential pulse adsorptive stripping voltammetry (DPAdSV), square wave anodic stripping voltammetry (SWASV) and linear sweep anodic stripping voltammetry (LSASV).

Mercury has a detection limit ( $3\sigma$ ) of 1 nM and its peak current rises linearly with increasing concentrations up to 400 nM (Figure 11(g)). The observed detection limit of this study is lower than the recommended maximum threshold limit (2 ppb) for drinking water by WHO. Therefore, the electrode exhibited a wide linear range and, a lesser detection limit. The potential of the prepared sensor electrode was compared with a few other existing electrodes (Table 4) utilized for the determination of Hg. The table proves that the proposed interface has a lesser detection limit than others. Hence the prepared sensor electrode possibly be an alternative tool to the existing sensors in industrial needs for repetitive monitoring of toxic Hg present at traces of ultra level.

**Table 4:** Comparison of existing sensors for mercury with the proposed sensor.

Various Electrode	Method	PCT (s)	Limit of Detection (LOD/nM)	Ref.
GC-MWCNTS-DHP	SWASV	300	32	[60]
GC-MBT polymer	DPASV	300	40	[61]
GC-Au	DPASV	120	0.2	[60]
GC-MWCNTs-Chi	LSASV	120	2.4	[61]
CPE-S-Nanoporous	DPASV	450	8	[63]
GC-MWCNTs	DPASV	300	20	[64]
EG-MBT	DPASV	180	1	This work

### 3.4.4 Interference study

Real samples typically consist of a large number of toxic compounds with an active potential equal to the analyte's potential. This means that there is a high likelihood that these foreign substances will interfere with the analyte while the potential is being scanned across the window. Therefore, it is adequate to check the possibility and the extent of interference of interfering species during the determination of mercury. In view of this, the interference study was conducted by adding cations or anions by varying their concentrations into the electrochemical cell containing

Hg (100 nm.) in electrochemical analysis. The various interfering ions with their maximum concentration levels (tolerance limit) in our work were tabulated (Table 5). We can understand that the sensor electrode showed very little interference from almost all of the common ions because of its specific and selective interaction with mercury. It can be concluded that the prepared sensor electrode could successfully be utilized in the sensing of Hg from a various environmental field.

**Table 5:** Interference analysis.

Interfering Common Ions (nM)	Tolerance Limits
Cd <sup>2+</sup> , Zn <sup>2+</sup> , Fe <sup>2+</sup> , Ag <sup>+</sup> , Ni <sup>2+</sup> , Cu <sup>2+</sup> , Pb <sup>2+</sup> , Co <sup>2+</sup>	480
Na <sup>+</sup> , K <sup>+</sup> , Cs <sup>+</sup>	500
Co <sup>2+</sup> , Cr <sup>3+</sup> , Mg <sup>2+</sup> , Ca <sup>2+</sup> , Ba <sup>2+</sup> , Fe <sup>3+</sup> , Be <sup>2+</sup> , As <sup>3+</sup>	450
CO <sub>3</sub> <sup>2-</sup> , C <sub>2</sub> O <sub>4</sub> <sup>2-</sup> , Cl <sup>-</sup> , F <sup>-</sup> , I <sup>-</sup> , SO <sub>3</sub> <sup>2-</sup> , SO <sub>4</sub> <sup>2-</sup> , NO <sub>3</sub> <sup>-</sup> , NO <sub>2</sub> <sup>-</sup>	390

### 3.4.5 The real samples study

The real time sample of water collected from tap, lake, and industrial waste effluents from various plating industries like chromium and electroplating as well as textile industries in tumkur surroundings were compared and validated for the Hg levels by the prepared electrode. After the concertation spiking of Hg, the recovery study of all samples was also listed in Table 6. The World Health Organisation and the US Environmental Protection Agency suggest that the maximum permitted levels of mercury in drinking water be 0.001 and 0.002 mg/L, respectively. The conversion factor indicates that 1 nM is equal to 0.4 mg/dL, or 4 mg/L. Therefore, the mercury content of tap water is 5.6 mg/L, industrial water (Antharasanahalli Industrial effluent, Tumakuru.) is 556 mg/L, lake water (Tumakuru & Amanikere) is 612 mg/L, and textile industrial effluent has a very high mercury content of 736 mg/L. From this comparison, we can suggest that ZnO/g-C<sub>3</sub>N<sub>5</sub> is a novel nanomaterial for sensing heavy metal ions such as mercury in different water resources.

**Table 6:** Application to real samples.

Collected sample	Initially present Hg (nM)	Addition of Hg (nM)	Total Hg (M)	Recovery (%)
Tap water	ND	80	81.4	101.78
Industrial water	140	80	219	99.54
Lake water	151	80	233	100.86
Textile industrial effluent	180	80	264	101.53

ND - Not detected.

## 5 Conclusions

The work showed successful synthesis of ZnO/g-C<sub>3</sub>N<sub>5</sub> S-scheme heterojunction nano-composite by hydrothermal-ultrasonication method for Rh B degradation and Hg detection. TEM studies show the clear existence of boundaries as well as stacking between ZnO and g-C<sub>3</sub>N<sub>5</sub>, and UV-DRS studies show the red shift confirms the possibility of S-scheme heterojunction over ZnO/g-C<sub>3</sub>N<sub>5</sub>. This heterojunction supports the absorption of visible light and conversion for the efficient separation which promotes photogenerated carrier. The peak positions from the XPS spectrum of Zn2p and O1s show high binding energy when compared to the ZnO/g-C<sub>3</sub>N<sub>5</sub> conventional XPS spectrum. In addition, the C1 and N1 peak positions show low binding energy. The charge transfer mechanism through the S-scheme of ZnO/g-C<sub>3</sub>N<sub>5</sub> is directly supported by this data, which shows that photoelectrons migrate from ZnO to g-C<sub>3</sub>N<sub>5</sub>. The ZnO/g-C<sub>3</sub>N<sub>5</sub> has enhanced RhB photodegradation to 97.53%. The degradation stability was retained for up to 5 cycles, signifying that ZnO/g-C<sub>3</sub>N<sub>5</sub> better stable material. The electrochemical studies show the sensor detection of Hg at low levels. This study further proves the least interference of ions during the detection.

## Acknowledgement

We would like to express our deepest regards to the Centre for Advanced Materials & Technology, M.S. Ramaiah Institute of Technology, Bangalore, India, for their support and help toward characterization analysis.

## Author Contributions

G.K.: Conceptualization, supervision, Methodology, Formal analysis, Investigation, resources, writing original draft, and writing-review & editing; R.B.N.: Conceptualization, Methodology, writing original draft, Writing-review & editing; M.S: Investigation, Writing-review & editing, K.K. and R.G.K.: Formal analysis, Investigation; A.P.C.: Formal analysis, Investigation; N.K.: Investigation, R.G.K.: Formal analysis; A.T.: Manuscript refinement, editing, data curation, All authors have read and agreed to the published version of manuscript.



## Conflicts of Interest

Authors declare no conflicts of interest.

## References

- [1] Y. Luo, Q. Guo, J. Xu, H. Zhou, Z. Wang, and H. He, "Growth of BaTaO<sub>2</sub>N–BaNa<sub>0.25</sub>Ta<sub>0.75</sub>O<sub>3</sub> solid solution photocatalyst for visible light-driven Z-scheme overall water splitting," *Energy Material Advances*, vol. 2022, 2022, Art. no. 0003, doi: 10.34133/energymatadv.0003.
- [2] K. Gurushantha, K. Keshavamurthy, S. Meena, N. Kottam, M. N. Manjunatha, S. Malini, S. Shashidhar, G. Shobha, and T. Ramakrishna, "Synthesis of heterojunction nanocomposites ZnFe<sub>2</sub>O<sub>4</sub>/ZnO/Nb<sub>2</sub>O<sub>5</sub> for photocatalytic, capacitor and antibacterial applications," *Inorganic Chemistry Communications*, vol. 162, 2024, Art. no. 112126, doi: 10.1016/j.inoche.2024.112126.
- [3] A. Thakur and H. Kaur, "Response surface optimization of Rhodamine B dye removal using paper industry waste as adsorbent," *International Journal of Industrial Chemistry*, vol. 8, pp. 175–186, 2017, doi: 10.1007/s40090-017-0113-4.
- [4] H. Nezzal, S. Rahmane, E. G. Temam, M. Al-Abri, H. H. Kyaw, B. Gasmi, M. Althamthami, H. B. Temam, and J. Hu, "Photo-deposition of AgO thin films on TiO<sub>2</sub> substrate for (PN) hetero-junction applications: Considering the degree of contamination," *Journal of Alloys and Compounds*, vol. 1010, 2025, Art. no. 177331, doi: 10.1016/j.jallcom.2024.177331.
- [5] N. Mokrani, E. G. Temam, H. B. Temam, H. Barkat, M. Althamthami, "Enhancing water purification with light-activated strontium-doped ZnO thin films," *Advances in Natural Sciences: Nanoscience and Nanotechnology*, vol. 16, no. 1, 2025, Art. no. 015012, doi: 10.1088/2043-6262/ada005.
- [6] B. Zhu, J. Sun, Y. Zhao, L. Zhang, and J. Yu, "Construction of 2D S-scheme heterojunction photocatalyst," *Advanced Materials*, vol. 36, no. 8, 2024, Art. no. 2310600, doi: 10.1002/adma.202310600.
- [7] H. Houda, G. T. Elhachmi, M. Althamthami, H. B. Temam, and S. Rahmane, "Property analysis of  $\beta$ -tetragonal bismite thin films: Varied concentrations and enhanced photocatalytic efficiency," *Iranian Journal of Materials Science & Engineering*, vol. 21, no. 4, 2024, doi: 10.22068/ijmse.3514
- [8] B. N. Roopashree, K. Gurushantha, Kottam Nagaraju, and S. Meena, "Recent review on s-scheme photocatalysis," *Water, Air, & Soil Pollution*, vol. 235, no. 9, pp. 1–25, 2024, doi: 10.1007/s11270-024-07376-y
- [9] N. Srinatha, S. S. Reddy, M. Al-Dossari, K. Gurushantha, N. S. A. EL-Gawaad, S. O. Manjunatha, K. J. R. Kumar, M. R. S. Kumar, V. B. Tangod, and A. Madhu, "Effect of aliovalent substitution in the band structure engineered Ca<sup>2+</sup>-doped LaFeO<sub>3</sub> nanoparticles for visible light-induced photocatalytic studies," *Ceramics International*, vol. 50, no. 1, pp. 1836–1848, 2024, doi: 10.1016/j.ceramint.2023.10.283.
- [10] H. Nayak and B. Padhi, "Photocatalytic decomposition of methylene blue over nanosized Ca<sup>2+</sup> doped LaMnO<sub>3</sub> under visible light irradiation," *Asian Journal of Applied Chemistry Research*, vol. 13, no. 3, pp. 39–49, 2023, doi: 10.9734/AJACR/2023/v13i3247.
- [11] T. Xu, R. Wang, C. Gu, and T. Jiang, "Recyclable detection of gefitinib in clinical sample mediated by multifunctional Ag-anchored g-C<sub>3</sub>N<sub>4</sub>/MoS<sub>2</sub> composite substrate," *Spectrochimica Acta Part A: Molecular and Biomolecular Spectroscopy*, vol. 299, 2023, Art. no. 122801, doi: 10.1016/j.saa.2023.122801.
- [12] Z. Wang, Z. Huang, J. Yu, X. Shao, W. Peng, J. Yu, and Y. Jiang, "Growth of Ag/g-C<sub>3</sub>N<sub>4</sub> nanocomposites on nickel foam to enhance photocatalytic degradation of formaldehyde under visible light," *Journal of Environmental Sciences*, vol. 137, pp. 432–442, 2024, doi: 10.1016/j.jes.2023.02.003.
- [13] O. A. Oyewo, S. Ramaila, and L. Mavuru, "Adsorption and photocatalytic removal of murexide using ZnO/rGO and ZnO/g-C<sub>3</sub>N<sub>4</sub> composites," *Inorganic Chemistry Communications*, vol. 151, 2023, Art. no. 110601, doi: 10.1016/j.inoche.2023.110601.
- [14] Y. He, H. Hu, J. Wang, X. Wang, M. Sun, C. Tian, and C. Deng, "Fabrication of multi-scale CdS/ZnO heteroarchitectures with boosted dual photocatalytic activities for hydrogen generation and organic dye degradation under solar light," *Materials Research Bulletin*, vol. 162, 2023, Art. no. 112180, doi: 10.1016/j.materresbull.2023.112180.
- [15] X. Xie and E. Bakker, "Ion selective optodes: From the bulk to the nanoscale," *Analytical and*

- Bioanalytical Chemistry*, vol. 407, pp. 3899–3910, 2015, doi: 10.1007/s00216-014-8413-4.
- [16] E. Sacher and R. França, “Dental biomaterials,” *World Scientific*, vol. 2, 2018, doi: 10.1142/10589.
- [17] S. Chilov, “Determination of small amounts of mercury,” *Talanta*, vol. 22, no. 3, pp. 205–232, 1975, doi: 10.1016/0039-9140(75)80059-2.
- [18] F. Edition, “Guidelines for drinking-water quality,” *WHO Chronicle*, vol. 38, no. 4, pp. 104–108, 2011.
- [19] M. R. Rahman, T. Okajima, and T. Ohsaka, “Selective detection of As (III) at the Au (111)-like polycrystalline gold electrode,” *Analytical Chemistry*, vol. 82, no. 22, pp. 9169–9176, 2010, doi: 10.1021/ac101206j.
- [20] V. Adimule, R. Keri, S. Rajendrachari, P. Kendrekar, and C. V. Kulkarni, “Highly photoluminescence and wide band gap insulating metal hybrid nanoparticles array of samarium-doped SrO: CoO: Synthesis, characterizations and sensor characteristics,” *Journal of Materials Science: Materials in Electronics*, vol. 34, no. 5, p. 442, 2023, doi: 10.1007/s10854-023-09899-2.
- [21] D. W. M. Arrigan, “Tutorial review. Voltammetric determination of trace metals and organics after accumulation at modified electrodes,” *Analyst*, vol. 119, no. 9, pp. 1953–1966, 1994, doi: 10.1039/AN9941901953.
- [22] N. A. Bohari, S. Siddiquee, S. Saallah, M. Misson, and S. E. Arshad, “Electrochemical behaviour of real-time sensor for determination mercury in cosmetic products based on PANI/MWCNTs/AuNPs/ITO,” *Cosmetics*, vol. 8, no. 1, p. 17, 2021, doi: 10.3390/cosmetics8010017.
- [23] H. Barkat, E. G. Temam, H. Ben Temam, N. Mokrani, S. Rahmane, and M. Althamthami, “Enhancing sunlight-driven photocatalysis: High transparency and hydrophilic advancements in Ba-Doped ZnO thin films,” *Journal of Materials Engineering and Performance*, pp. 1–14, 2024, doi: 10.1007/s11665-024-10126-0.
- [24] N. Mokrani, E. G. Temam, H. Barkat, H. B. Temam, S. Rahmane, and M. Althamthami, “Boosting photocatalytic stability: Hydrophilic Sr-doped ZnO thin films prepared via the SILAR method for enhanced performance over multiple cycles,” *Physica Scripta*, vol. 99, no. 9, 2024, Art. no. 0959a4, doi: 10.1088/1402-4896/ad6ffb.
- [25] J. Jia, L. Huang, Y. Yan, H. Wang, M. Tian, and J. Jiang, “A novel S-scheme ZnO/Ce-g-C<sub>3</sub>N<sub>5</sub> heterojunctions with enhanced photocatalytic activity,” *Journal of Sol-Gel Science and Technology*, vol. 111, no. 3, pp. 819–833, 2024, doi: 10.1007/s10971-024-06491-w.
- [26] P. Kumar, E. Vahidzadeh, U. K. Thakur, P. Kar, Kazi M. Alam, A. Goswami, N. Mahdi, K. Cui, G. M. Bernard, V. K. Michaelis, and K. Shankar, “C<sub>3</sub>N<sub>5</sub>: A low bandgap semiconductor containing an azo-linked carbon nitride framework for photocatalytic, photovoltaic and adsorbent applications,” *Journal of the American Chemical Society*, vol. 141, no. 13, pp. 5415–5436, 2019, doi: 10.1021/jacs.9b00144.
- [27] J. Liu, S. Wang, C. Zhao, and J. Zheng, “Engineered g-C<sub>3</sub>N<sub>5</sub>-based nanomaterials for photocatalytic energy conversion and environmental remediation,” *Nanomaterials*, vol. 13, no. 3, p. 499, 2023, doi: 10.3390/nano13030499.
- [28] A. Singh and H. L. Vishwakarma, “Study of structural, morphological, optical and electroluminescent properties of undoped ZnO nanorods grown by a simple chemical precipitation,” *Materials Science-Poland*, vol. 33, no. 4, pp. 751–759, 2015, doi: 10.1515/msp-2015-0112.
- [29] M. Rostami, M. Jourshabani, F. Davar, G. M. Ziarani, and A. Badiie, “Black TiO<sub>2</sub>-g-C<sub>3</sub>N<sub>4</sub> heterojunction coupled with MOF (ZIF-67)-derived Co<sub>3</sub>S<sub>4</sub>/nitrogen-doped carbon hollow nanobox,” *Journal of the American Ceramic Society*, vol. 107, no. 2, pp. 719–735, 2024, doi: 10.1111/jace.19447.
- [30] E. Baladi, F. Davar, and A. Hojjati-Najafabadi, “Synthesis and characterization of g-C<sub>3</sub>N<sub>4</sub>-CoFe<sub>2</sub>O<sub>4</sub>-ZnO magnetic nanocomposites for enhancing photocatalytic activity with visible light for degradation of penicillin G antibiotic,” *Environmental Research*, vol. 215, 2022, Art. no. 114270, doi: 10.1016/j.envres.2022.114270.
- [31] G. Xiong, U. Pal, J. G. Serrano, K. B. Ucer, and R. T. Williams, “Photoluminescence and FTIR study of ZnO nanoparticles: The impurity and defect perspective,” *Physica Status Solidi C*, vol. 3, no. 10, pp. 3577–3581, 2006, doi: 10.1002/pssc.200672164.
- [32] M. H. Sayadi, S. Ghollasimood, N. Ahmadpour, and S. Homaeigohar, “Biosynthesis of the ZnO/SnO<sub>2</sub> nanoparticles and characterization of their photocatalytic potential for removal of organic water pollutants,” *Journal of Photochemistry and Photobiology A: Chemistry*, vol. 425, 2022, Art. no. 113662, doi: 10.1016/j.jphotochem.2021.1136620.



- [33] H. Wang, M. Li, Q. Lu, Y. Cen, Y. Zhang, and S. Yao, "A mesoporous rod-like g-C<sub>3</sub>N<sub>5</sub> synthesized by salt-guided strategy: As a superior photocatalyst for degradation of organic pollutant," *ACS Sustainable Chemistry & Engineering*, vol. 7, no. 1, pp. 625–631, 2018, doi: 10.1021/acssuschemeng.8b04182.
- [34] J. H. Zheng, Q. Jiang, and J. S. Lian, "Synthesis and optical properties of flower-like ZnO nanorods by thermal evaporation method," *Applied Surface Science*, vol. 257, no. 11, pp. 5083–5087, 2011, doi: 10.1016/j.apsusc.2011.01.025.
- [35] J. Chastain and R. C. King Jr, "Handbook of X-ray photoelectron spectroscopy," *Perkin-Elmer Corporation*, vol. 40, p. 221, 1992.
- [36] J. Das, S. K. Pradhan, D. R. Sahu, D. K. Mishra, S. N. Sarangi, B. B. Nayak, S. Verma, and B. K. Roul, "Micro-Raman and XPS studies of pure ZnO ceramics," *Physica B: Condensed Matter*, vol. 405, no. 10, pp. 2492–2497, 2010, doi: 10.1016/j.physb.2010.03.020.
- [37] J. Lee, J. Chung, and S. Lim, "Improvement of optical properties of post-annealed ZnO nanorods," *Physica E: Low-dimensional Systems and Nanostructures*, vol. 42, no. 8, pp. 2143–2146, 2010, doi: 10.1016/j.physe.2010.04.013.
- [38] C. Fu, T. Wu, G. Sun, G. Yin, C. Wang, G. Ran, and Q. Song, "Dual-defect enhanced piezocatalytic performance of C<sub>3</sub>N<sub>5</sub> for multifunctional applications," *Applied Catalysis B: Environmental*, vol. 323, 2023, Art. no. 122196, doi: 10.1016/j.apcatb.2022.122196.
- [39] H. Wang, M. Li, Q. Lu, Y. Cen, Y. Zhang, and S. Yao, "A mesoporous rod-like g-C<sub>3</sub>N<sub>5</sub> synthesized by salt-guided strategy: As a superior photocatalyst for degradation of organic pollutant," *ACS Sustainable Chemistry & Engineering*, vol. 7, no. 1, pp. 625–631, 2018, doi: 10.1021/acssuschemeng.8b04182.
- [40] S. Liu, Y. Bu, S. Cheng, and R. Tao, "Synthesis of TiO<sub>2</sub>/g-C<sub>3</sub>N<sub>5</sub> heterojunction for photocatalytic degradation of methylene blue wastewater under visible light irradiation: Mechanism analysis," *Diamond and Related Materials*, vol. 136, 2023, Art. no. 110062, doi: 10.1016/j.diamond.2023.110062.
- [41] Y. Liu, H. Liu, H. Zhou, T. Li, and L. Zhang, "A Z-scheme mechanism of N-ZnO/g-C<sub>3</sub>N<sub>4</sub> for enhanced H<sub>2</sub> evolution and photocatalytic degradation," *Applied Surface Science*, vol. 466, pp. 133–140, 2019, doi: 10.1016/j.apsusc.2018.10.027.
- [42] K. Yousra, E. G. Temam, R. Saâd, and H. Barkat, "Effect of film thickness on the electrical and the photocatalytic properties of ZnO nanorods grown by SILAR technique," *Physica Scripta*, vol. 98, no. 12, 2023, Art. no. 125954, doi: 10.1088/1402-4896/ad0ae7.
- [43] Y. Zhang, D. L. Liu, B. Y. Xiong, J. L. Li, Y. T. Li, Y. L. Zhou, A. S. Yang, and Q. P. Zhang, "Constructing WO<sub>3</sub>/TiO<sub>2</sub> heterojunction with solvothermal-sintering for enhanced photocatalytic activity under visible light irradiation," *Solid State Sciences*, vol. 131, 2022, Art. no. 106963, doi: 10.1016/j.solidstatesciences.2022.106963.
- [44] B. Li, B. Zhang, Y. Zhang, M. Zhang, W. Huang, C. Yu, J. Sun, J. Feng, S. Dong, and J. Sun, "Porous g-C<sub>3</sub>N<sub>4</sub>/TiO<sub>2</sub> S-scheme heterojunction photocatalyst for visible-light driven H<sub>2</sub>-production and simultaneous wastewater purification," *International Journal of Hydrogen Energy*, vol. 46, no. 64, pp. 32413–32424, 2021, doi: 10.1016/j.ijhydene.2021.07.090.
- [45] L. Zhang, J. Guo, B. Hao, and H. Ma, "WO<sub>3</sub>/TiO<sub>2</sub> heterojunction photocatalyst prepared by reactive magnetron sputtering for Rhodamine B dye degradation," *Optical Materials*, vol. 133, 2022, Art. no. 113035, doi: 10.1016/j.optmat.2022.113035.
- [46] F. H. AlHamedi, M. A. Rauf, and S. S. Ashraf, "Degradation studies of Rhodamine B in the presence of UV/H<sub>2</sub>O<sub>2</sub>," *Desalination*, vol. 239, no. 1–3, pp. 159–166, 2009, doi: 10.1016/j.desal.2008.03.016.
- [47] K. Gurushantha, K. S. Anantharaju, H. Nagabhushana, S. C. Sharma, Y. S. Vidya, C. Shivakumara, H. P. Nagaswarupa, S. C. Prashantha, and M. R. Anilkumar, "Facile green fabrication of iron-doped cubic ZrO<sub>2</sub> nanoparticles by *Phyllanthus acidus*: Structural, photocatalytic and photoluminescent properties," *Journal of Molecular Catalysis A: Chemical*, vol. 397, pp. 36–47, 2015, doi: 10.1016/j.molcata.2014.10.025.
- [48] A. Trenczek-Zajac, M. Synowiec, K. Zakrzewska, K. Zazakowny, K. Kowalski, A. Dziedzic, and M. Radecka, "Scavenger-supported photocatalytic evidence of an extended type I electronic structure of the TiO<sub>2</sub>@Fe<sub>2</sub>O<sub>3</sub> interface," *ACS Applied Materials &*

- Interfaces*, vol. 14, no. 33, pp. 38255–38269, 2022, doi: 10.1021/acsami.2c06404.
- [49] Y. Narita, K. Nishi, T. Matsuyama, and J. Ida, “Reusable isotype heterojunction g-C<sub>3</sub>N<sub>4</sub>/alginate hydrogel spheres for photocatalytic wastewater treatment,” *RSC advances*, vol. 14, no. 29, pp. 20898–20907, 2024, doi:10.1039/D4RA02876G.
- [50] E. G. Temam, F. Djani, S. Rahmane, H. B. Temam, and B. Gasmi, “Photocatalytic activity of Al/Ni doped TiO<sub>2</sub> films synthesized by sol-gel method: dependence on thickness and crystal growth of photocatalysts,” *Surfaces and Interfaces*, vol. 31, 2022, Art. no. 102077, doi: 10.1016/j.surfin.2022.102077.
- [51] Y. Wang, Y. He, Y. Chi, P. Yin, L. Wei, W. Liu, X. Wang, H. Zhang, and H. Song, “Construction of S-scheme pn heterojunction between protonated g-C<sub>3</sub>N<sub>4</sub> and α-MnS nanosphere for photocatalytic H<sub>2</sub>O<sub>2</sub> production and in situ degradation of oxytetracycline,” *Journal of Environmental Chemical Engineering*, vol. 11, no. 3, 2023, Art. no. 109968, doi: 10.1016/j.jece.2023.109968.
- [52] C. Yang, J. Yang, S. Liu, M. Zhao, X. Duan, H. Wu, L. Liu, W. Liu, J. Li, S. Ren, and Q. Liu, “Constructing C–O bridged CeO<sub>2</sub>/g-C<sub>3</sub>N<sub>4</sub> S-scheme heterojunction for methyl orange photodegradation: Experimental and theoretical calculation,” *Journal of Environmental Management*, vol. 335, 2023, Art. no. 117608, doi: 10.1016/j.jenvman.2023.117608.
- [53] K. Bi, X. Qin, S. Cheng, and S. Liu, “ZnO/g-C<sub>3</sub>N<sub>4</sub> S scheme photocatalytic material with visible light response and enhanced photocatalytic performance,” *Diamond and Related Materials*, vol. 137, 2023, Art. no. 110143, doi: 10.1016/j.diamond.2023.110143.
- [54] J. Liu, G. Zhu, M. Chen, X. Ma, J. Yang, “Fabrication of electrospun ZnO nanofiber-modified electrode for the determination of trace Cd (II),” *Sensors and Actuators B: Chemical*, vol. 234, pp. 84–91, 2016, doi: 10.1016/j.snb.2016.04.073.
- [55] M. Amiri, H. Salehniya, and A. Habibi-Yangjeh, “Graphitic carbon nitride/chitosan composite for adsorption and electrochemical determination of mercury in real samples,” *Industrial & Engineering Chemistry Research*, vol. 55, no. 29, pp. 8114–8122, 2016, doi: 10.1021/acs.iecr.6b01699.
- [56] A. Das and M. K. Adak, “Kinetic and mechanistic way for photocatalytic degradation of pollutants from textile wastewater by graphene oxide supported nanocomposite,” *Next Materials*, vol. 3, 2024, Art. no. 100153, doi: 10.1016/j.nxmte.2024.100153.
- [57] M. T. D. Español, E. J. G. Garcia, L. A. V. Maligaya, C. M. S. Santos, J. A. H. Santos, N. G. Suarnaba, R. V. C. Rubi, and R. Raguindin, “Ultrasound-assisted biomimetic synthesis of mof-hap nanocomposite via 10xsbf-like for the photocatalytic degradation of metformin,” *Applied Science and Engineering Progress*, vol. 17, no. 2, 2024, Art. no. 7251, doi: 10.14416/j.asep.2023.11.002.
- [58] T. Q. Thao, N. T. T. Hien, P. T. Lam, N. N. Huy, P. T. Thi, N. T. Thanh, P. P. Toan, L. T. Thich, and N. T. Thuy, “Exploring the mechanism for the photocatalytic degradation of oxytetracycline in water using TiO<sub>2</sub> and supplementary oxidants,” *Applied Science and Engineering Progress*, vol. 18, no. 3, 2025, Art. no. 7651, doi: 10.14416/j.asep.2024.11.007.
- [59] N. Kottam, K. R. Jammula, S. J. Shivaram, B. A. Rajappa, P. Narayanappa, S. S. P. Nair, and A. Tawai, “Design and development of g-C<sub>3</sub>N<sub>4</sub>/ZnO/CdS ternary photocatalyst for the removal of environmentally hazardous organic dyes under visible light,” *Applied Science and Engineering Progress*, vol. 18, no. 3, 2025, Art. no. 7654, doi: 10.14416/j.asep.2024.11.008.
- [60] F. B. Sousa, Maria, É. J. Dallan, S. B. Yamaki, and R. Bertazzoli, “Preparation of polymer-coated electrodes containing metal ions complexing sites by electropolymerization of 2-mercaptobenzimidazole and 2-mercaptobenzothiazole on glassy carbon,” *Electroanalysis*, vol. 9, no. 8, pp. 614–618, 1997, doi: 10.1002/elan.1140090807.
- [61] R. G. Kempgowda and P. Malingappa, “Diazonium functionalized exfoliated graphitic carbon as a binderless and covalently modified electrochemical interface for mercury sensing,” *Sensors and Actuators B: Chemical*, vol. 186, pp. 478–485, 2013, doi: 10.1016/j.snb.2013.06.028.
- [62] H. Yi, “Anodic stripping voltammetric determination of mercury using multi-walled carbon nanotubes film coated glassy carbon electrode,” *Analytical and Bioanalytical Chemistry*, vol. 377, pp. 770–774, 2003, doi: 10.1007/s00216-003-2136-2.



- [63] B. C. Janegitz, L. C. S. Figueiredo-Filho, L. H. Marcolino-Junior, S. P. Souza, E. R. Pereira-Filho, and O. Fatibello-Filho, "Development of a carbon nanotubes paste electrode modified with crosslinked chitosan for cadmium (II) and mercury (II) determination," *Journal of Electroanalytical Chemistry*, vol. 660, no. 1, pp. 209–216, 2011, doi: 10.1016/j.jelechem.2011.07.001.
- [64] O. Abollino, A. Giacomino, M. Malandrino, G. Piscionieri, and E. Mentasti, "Determination of mercury by anodic stripping voltammetry with a gold nanoparticle-modified glassy carbon electrode," *Electroanalysis: An International Journal Devoted to Fundamental and Practical Aspects of Electroanalysis*, vol. 20, no. 1, pp. 75–83, 2008, doi: 10.1002/elan.200704044.